

Detector optimisation for future linear collider

Boruo Xu
of King's College

A dissertation submitted to the University of Cambridge
for the degree of Doctor of Philosophy

Abstract

This is my abstract. To be or not to be.

Declaration

This dissertation is the result of my own work, except where explicit reference is made to the work of others, and has not been submitted for another qualification to this or any other university. This dissertation does not exceed the word limit for the respective Degree Committee.

Boruo Xu

Acknowledgements

Of the many people who deserve thanks, some are particularly prominent, such as my supervisor. . .

Preface

This will be my preface. Where is Wolly?

Contents

1	Let's make introduction great again	1
2	Detector	3
3	Reconstruction	5
3.1	Reconstruction overall	5
3.2	Pandora	5
3.2.1	Cone clustering	5
4	Analysis technique	7
4.1	Jet algorithm	7
4.1.1	k_t algorithm	8
4.1.2	Durham algorithm	9
4.1.3	Jet algorithm for CLIC	9
4.1.4	y parameter	9
4.2	Flavour tagging	10
4.3	Multivariate analysis	11
4.3.1	Choice of models	11
4.3.2	Rectangular Cut	12
4.3.3	Projective Likelihood	12
4.3.4	Boosted decision tree	13
4.3.5	Optimisation and overfitting	13
4.4	Event shape	13
4.4.1	Jargons	13
5	Photon Reconstruction	15
6	Tau Lepton Final State Separation	17

7 Double Higgs Bosons Analysis	19
7.1 Motivation	19
7.2 Theory	19
7.3 Analysis Straggly Overview	20
7.4 Monte Carlo Sample Generation	20
7.5 Physics object and event reconstruction	21
7.5.1 Electron and muon identification	23
7.5.2 Tau identification	25
7.5.3 Very forward electron identification	27
7.5.4 Other lepton identification processors	27
7.6 Jet reconstruction	28
7.6.1 Jet reconstruction optimisation	28
7.6.2 Jet flavour tagging	35
7.6.3 Jet pairing	35
7.7 Pre-selection	36
7.7.1 Discriminative pre-selection cuts	37
7.7.2 Sanity cuts	42
7.7.3 Mutually exclusive cuts for $HH \rightarrow b\bar{b}W^+W^-$ and $HH \rightarrow b\bar{b}b\bar{b}$. . .	42
7.8 Discriminative Variables	43
7.9 Multivariate analysis	46
7.10 Signal selection results	46
7.11 Couplings extration	46
Bibliography	49
List of figures	51
List of tables	53

*“Two bags of pork scratchings are worth
a bag of gold.”*

— Joris the Dutch

Chapter 1

Let's make introduction great again

“Introduction means introdcution”

— Theresa Trump

Introduction

Chapter 2

Detector

“ILC will be built next year”

— Mysterious person

overall

ILC

CLIC

calorimeter

ECal

HCal

Muon chamber

Forward detector

Tracker

Chapter 3

Reconstruction

“How to open a pandora box?”

— A wise Chinese

3.1 Reconstruction overall

digitisation tracking

3.2 Pandora

Track quality cuts

3.2.1 Cone clustering

Cone clustering is used in PandoraPFA for grouping calorimeter hits, within a opening angle of the seed hit. Because the direction of particle flows is largely unchanged from the originated particle, whether it is a electromagnetic shower, QCD radiation or hadronisation, these cone clusters have similar direction and energy to the originated particle.

Typically a high energy calorimeter hit will be chosen as a “seed”. A cone with a specified opening angle and depth will be formed around the seed. The four-momentum of calorimeter hits sum to the cone’s four-momentum.

These cone clustering algorithms are widely used in the calorimeter in PandoraPFA, and they produce basic working objects, Clusters.

Iterative track-cluster association

Photon, passage through matter

Muon ID

Fragmentation

Chapter 4

Analysis technique

“In preparing for battle I have always found that plans are useless, but planning is indispensable.”

— Dwight D. Eisenhower

Automated analysis is the only way to deal with the vast amount of data generated in the high energy physics. In the last chapter we described the automated reconstruction tools in details. This chapter is dedicated to the common automated analysis tools and techniques, which will be used in the analysis described in subsequent chapters.

For the linear collider, thanks to the high granular calorimeter, the starting point for analysis would be individual Particle Flow Objects, as well as individual tracks. Each of the PFOs encodes four-momentum and position information. For tracks, they would have momentum and position information.

However, sometimes it is interesting to group PFOs and tracks into jets, where a jet is the result of hadronisation process from high energy particles like quarks or gluons.

4.1 Jet algorithm

A jet is typically a visually obvious structure in a event display. The momentum and the direction of a jet tend to resemble the originated particle. Despite the relative easiness of identifying jets visually, it presents a challenge for a pattern recognition program to identify jets effectively and efficiently.

Early work on jet finding started in 1977 [1], where later development can be found in reviews [2–4].

There are two large families of jet finding algorithm, cone based algorithm, and sequential combination algorithm. Cone based algorithm is briefly discussed in section 3.2.1.

Sequential combination algorithm typically calculate a pair-wise distance metric. Pairs with the smallest metric will be combined. The metric will be calculated and updated, and a pair with smallest metric will be combined. This procedure will be repeated until some stopping criterion are satisfied.

The chosen jet algorithm implementation is FastJet C++ software package [5, 6], providing a wide range of jet finding algorithms. The implementation in Marlin software package is called MarlinFastJet. The symbols in the subsequent discussion about specific jet algorithms will follow [5]

4.1.1 k_t algorithm

One of the common sequential combination algorithms for $p\bar{p}$ collider experiment, is longitudinally-invariant k_t algorithm [7, 8]. In the inclusive variant, The symmetrical pair-wise distance metric between particle i and j , and the beam distance, are defined as

$$d_{ij} = d_{ji} = \min(p_{Ti}^2, p_{Tj}^2) \frac{\Delta R_{ij}^2}{R^2}, \quad (4.1)$$

$$d_{iB} = p_{Ti}^2, \quad (4.2)$$

where p_{Ti} is the transverse momentum of particle i with respect to the beam (z) direction, and ΔR_{ij}^2 is the measurement of angular separation of particle i and j . Formally $\Delta R_{ij}^2 = (y_i - y_j)^2 + (\phi_i - \phi_j)^2$, where $y_i = \frac{1}{2} \ln \frac{E_i + p_{zi}}{E_i - p_{zi}}$ and ϕ_i are particle i 's rapidity and azimuthal angle. R is a free parameter controlling the jet radius.

If $d_{ij} < d_{iB}$, particle i and j are merged, with the four-momentum of particle i updated as the sum. Otherwise, particle i is set to be a final jet, and delete from the particle list. The above procedure is repeated until no particle left.

The exclusive variant is similar. First difference is that when $d_{iB} < d_{ij}$, the particle i is discarded and part of the beam jet. The second difference is that when both d_{ij} and d_{iB} are above some threshold, d_{cut} , the clustering will stop. In practise, exclusive mode

allows a specified number of jets to be found, which will automatically choose the d_{cut} . The inclusive mode would find as many jets as the algorithm allows.

4.1.2 Durham algorithm

Durham algorithm [9], also known as $e^-e^+ k_t$ algorithm, is commonly used e^-e^+ collider experiment. It has a single distance metric:

$$d_{ij} = 2 \min(E_i^2, E_j^2)(1 - \cos(\theta_{ij})), \quad (4.3)$$

where E_i is the energy of particle i . θ_{ij} is the polar angle difference between particle i and j . Durham algorithm can only be run at exclusive mode, which means that the clustering will stop when d_{ij} is above some threshold, d_{cut} .

Comparing to k_t algorithm, it uses energy instead of p_T in the distance metric, and it did not have a beam jet. This is because that for the e^-e^+ collider in the past, the beam induced background was not severe and collisions energy is known, \sqrt{s} .

4.1.3 Jet algorithm for CLIC

Although CLIC is a e^-e^+ collider, the significant beam-induced background adds a large amount of energy from $\gamma\gamma \rightarrow \text{hadrons}$ process. Therefore, traditional e^-e^+ jet algorithms, like Durham algorithm, is not suitable for CLIC environment. Studies have shown that jet algorithms for $p\bar{p}$ collider have better performance [10, 11].

A more recent attempt at marrying merits from both Durham and k_t algorithms has resulted in Valencia jet algorithm [12]. It had shown promising improvement comparing to k_t algorithm.

4.1.4 y parameter

y parameter is a commonly used quantity to describe the transition of exclusive jet algorithm going from N clustered jets to $N+1$ clustered jets. For example, y_{23} would be the d_{cut} value for an exclusive jet algorithm, above which the jet algorithm returns 2 jets, below which the jet algorithm returns 3 jets.

Numerically y parameter is often much smaller than one. A typically way to convert the small number to a human acceptable range is to take the minus logarithm of the number.

4.2 Flavour tagging

The latest software package for jet flavour tagging is LCFIPlus [13]. It is based on the LCFIVertex package, which was used in the simulation studies for ILC Letter of Intent [14, 15] and CLIC Concept Design Report [10]. Current software is built in mind of a future e^-e^+ collider. Although the software is modular, it will be described in order that it will be used in a physics analysis,

The vertex finding algorithms perform vertex fitting and identify primary and secondary vertex. There is a “V0” particle rejection, which is when neutral particles decay or convert into a pair of charged tracks. The topology is similar to the decay of b or c hadrons. Hence it is important to remove the V0 particles to improve the heavy quark flavour tagging.

Jet clustering ensures that the secondary vertices and the muons identified from semileptonic decay are combined. Therefore, it is consistent with the hadronic decay. Jet algorithms used are Durham and Durham modified algorithms.

Vertices are refined to improve the b jet identification from c jet. Two vertices is strongly correlated to a b jet. Hence the vertices refining will reconstruct as many secondary vertices correctly as possible.

The final flavour tagging of the jet is done using multivariate analysis, which will be discussed in section 4.3. Using TMVA software package [16], Boosted Decision Tree classifier is used. A series of flavour sensitive variables are calculated, and the classification is divided four sub-set: jet with zero, one, or two properly reconstructed vertices, or a single-track pseudovortex. For each sub-set, a jet can either be a b jet, a c jet, or a light flavour quark jet (u , d or s). The multiclass classifier’s response is normalised across different sub-set, and they will be referred in the subsequent physics analysis as the tag value.

4.3 Multivariate analysis

Multivariate analysis (MVA) has become increasingly common in high energy physics. MVA can be viewed as an advanced tool for regression or classification. Comparing to the traditional cut based method, modern machine learning technique offers much improvement in data analysis.

Software package for MVA used throughout this document is TMVA [16].

A typical machine learning MVA classification involves two classes, also known as signal and background. A machine learning model, called classifier in TMVA, needs to be trained with training data. The model requires a set of discriminative variables, which should separate signal from background. The trained model will be applied onto the testing data, for signal extraction. Response of the model could be signal/background, or be a number in a continuous spectrum, where the user decides the value to separate signal from background.

Strictly, there should be three statistically independent samples for the MVA. One sample is for the training. Another sample for the validation, including optimisation and checking for overfitting. The last sample is for testing. However, due to technical reason, sometimes the same sample is used for the validation and the testing.

This classification scheme can be easily extended to multiple classes, implemented in TMVA with multiclass class.

4.3.1 Choice of models

The model, known as the classifier in TMVA, can be as simple as cut based, likelihood or linear regression. It can be complicated as non linear tree, non linear neural network or support vector machine. Regardless of model complexity, the choice of most optimal classifier is often data driven. Also, given the free parameters in each model, the comparison between different models without individual tuning is not rigorous. Nevertheless, as researchers in the machine learning suggested, the boosted decision tree is probably the best out-of-the-box machine learning method. Neural network could potentially be better than the boosted decision, but it requires more tuning, and it is less intuitive to interpret the model. For these reasons, boost decision tree (BDT) is often the choice of

machine learning model in the high energy physics. And it is used in various physics analysis in this document.

Before describing BDT in detail, we will first visit the traditional rectangular cut model, and the Projective Likelihood method, which is used in the photon ID in the PandoraPFA.

4.3.2 Rectangular Cut

Probably the most intuitive model, the rectangular cut method optimise cuts to maximise some specific metric. The metric could be the signal efficiency for a particular background efficiency. Alternatively, the metric can be the significance, $\frac{S}{\sqrt{S+B}}$, where **S** and **B** are signal and background numbers, respectively.

Discriminative variables gives better separation power when they are gaussian-like and statistically independent. Therefore it is common to decoorelate the variables and gaussian transform them before using the rectangular cut MVA.

Because its simplicity, the cut method is often performed manual, much more often in the time pre-date the wide spread of machine learning methods. It is still commonly used for the pre-selection step before the MVA, and other simple usages. Unless specified, the optimal cuts proposed in this document for various physics analysis are found using the rectangular cut method manually.

4.3.3 Projective Likelihood

Projective likelihood model (PDE) is used in PandoraPFA for the photon ID due to its simplicity and low requirement on computing resources.

PDE implemented in the TMVA calculates the probability density for each discriminative variable, for signal and background. The overall signal and background likelihood are defined as products of the individual probability density. The likelihood ratio, **R**, is then defined as the signal likelihood over signal plus background likelihood.

TMVA implementation also fits an underlying function to the probability density. The PandoraPFA implementation simply uses binned likelihood ratio, **R**, as the output, due to the simplicity. The sub-categories for the PandoraPFA implementation are determined by the cluster energy.

Similarly to the rectangular cut method, PDE works better with decorrelated, gaussian like variables. The PandoraPFA implementation did not decorrelate nor transform the variables, to keep implementation fast.

4.3.4 Boosted decision tree

4.3.5 Optimisation and overfitting

BDT ?3likelihood Range, discrete Typical example: m in a good range log transformation

4.4 Event shape

Thrust Sphericity Aplanarity

4.4.1 Jargons

Signal Selection Efficiency Significance

q_l light quark light lepton

Thanks computing resources. i.e. ILC VO, CLIC grid, etc.

Chapter 5

Photon Reconstruction

“Photons have mass? I didn’t even know they were Catholic.”

— Woody Allen

Chapter 6

Tau Lepton Final State Separation

“MVA: Turn numbers into gold.”

— TMVA

Chapter 7

Double Higgs Bosons Analysis

“Two is better than one”

— Sir Steve Orange, 1785–1854

7.1 Motivation

Ha there is a higgs.

We found higgs. Higgs is cool. It explains mass.

Why double higgs. Double higgs coupling is unique to linear collider. It can reveal much about the BSM models.

Generator level study has performed. ILC has done this this and that. g_{HHH} in CLIC before

Here we do things differently. First subchannels, then extract both couplings simultaneously.

7.2 Theory

general higgs field

Lagrangian

current constraint

single higgs coupling measurement done in higgs

Double higgs measurement

The main mechanism for double Higgs production

7.3 Analysis Straggly Overview

Proof-of-principle study was performed at CLIC using CLIC_ILD detector model for $\sqrt{s} = 1.4 \text{ TeV}$ and 3 TeV . Simulated samples, including those containing double higgs production were used. Signal events, events with double higgs production, were selected via a set of carefully designed and complicated methods. g_{HHH} and g_{WWHH} are extracted simultaneously with template fitting with modified couplings samples.

7.4 Monte Carlo Sample Generation

Single channel is defined as $e^-e^+ \rightarrow HH\nu\bar{\nu}$. It is divided into sub-channel $HH \rightarrow b\bar{b}W^+W^-$ and $HH \rightarrow b\bar{b}b\bar{b}$ to allow closer examination and an improvement of signal selection when combined. In particular, I studied $HH \rightarrow b\bar{b}W^+W^-$ sub-channel.

Selected background samples, including processes initiated by photons, are considered in the analysis and listed in Table ???. These background were expected share similar topologies with the signal process. When describing a multi-quark final state, it is referring to all final states of the same number of quarks, including final states with possible additional neutrinos and or leptons. A multi-quark final state does not include higgs production, unless explicitly stated.

The usual two-quark and four-quark final states were considered. Since the significant presence of beamstrahlung, where photon produced due to the high electric field generated by the colliding beams, processes initiated by photons are also included.

Processes involving real photons from beamstrahlung (BS) and “quasi-real” photons are generated separately. For the “quasi-real” photon initiated processes, the Equivalent Photon Approximation (EPA) has been used.

Photon-electron/photon-photon interactions with four-quark final states were considered. Photon-electron interaction with two-quark final state, one Higgs, and one neutrino is considered. Photon-electron interaction with two-quark final state, one Higgs, and one lepton is not considered due to its negligible cross section.

Single higgs productions are not considered because topologies are very different to the single process. Six-quark final states were not considered due to computational limitation.

For processes involving Higgs production explicitly, simulated Higgs mass is 126 GeV. As multi-quark final state background samples could, in principle, contain double higgs production, they are generated with a Higgs mass of 14 TeV. This will produce negligible double higgs production cross section.

All samples are generated with WHIZARD 1.95 [1], taking into account the expected CLIC luminosity spectrum. PYTHIA 6.4 [2] tuned on LEP data [3] is used to describe fragmentation, hadronisation processes, and Higgs decays. TAUOLA [4] is used for τ lepton decays.

Simulation

For most background processes, events are simulated when invariant mass of quarks are above 50 GeV. For electron-photon interaction with four quarks and a neutrino final state, events are simulated when invariant mass of quarks are above 120 GeV. These limits are necessary to generate a large amount of background samples in a feasible time, without losing much signal samples.

Finally, the main beam induced background $\gamma\gamma \rightarrow \text{hadrons}$ is simulated and overlayed [5] to all samples according to the integration time of each subdetector.

7.5 Physics object and event reconstruction

Simulation is performed by MOKKA, interfacing GEANT 4. The reconstruction is done via Marlin in iLCSoft v01-16. Separate software package (processor) exists for identification of electrons, muons, taus, and jet reconstruction. New processors have been developed and existing processors have been optimised for a compromise of signal

Channel	$\sigma(\sqrt{s} = 1.4 \text{ TeV}) / \text{fb}$	$\sigma(\sqrt{s} = 3 \text{ TeV}) / \text{fb}$
$e^-e^+ \rightarrow HH\nu\bar{\nu}$	0.588	0.149
$e^-e^+ \rightarrow q_l q_l H\nu\bar{\nu}$	0.86	1.78
$e^-e^+ \rightarrow c\bar{c}H\nu\bar{\nu}$	0.36	1.12
$e^-e^+ \rightarrow b\bar{b}H\nu\bar{\nu}$	0.31	1.91
$e^-e^+ \rightarrow qq\bar{q}\bar{q}$	1245.1	546.5
$e^-e^+ \rightarrow qq\bar{q}q\ell\bar{\ell}$	62.1	169.3
$e^-e^+ \rightarrow qq\bar{q}q\ell\nu$	110.4	106.6
$e^-e^+ \rightarrow qq\bar{q}q\nu\bar{\nu}$	23.2	71.5
$e^-e^+ \rightarrow q\bar{q}$	4009.5	2948.9
$e^-e^+ \rightarrow q\bar{q}\ell\nu$	4309.7	5561.1
$e^-e^+ \rightarrow q\bar{q}\ell\bar{\ell}$	2725.8	3319.6
$e^-e^+ \rightarrow q\bar{q}\nu\nu$	787.7	1317.5
$e^-\gamma(\text{BS}) \rightarrow e^-\bar{q}q\bar{q}q$	1160.7	1268.7
$e^+\gamma(\text{BS}) \rightarrow e^+q\bar{q}q\bar{q}$	1156.3	1267.6
$e^-\gamma(\text{EPA}) \rightarrow e^-\bar{q}q\bar{q}q$	287.1	287.9
$e^+\gamma(\text{EPA}) \rightarrow e^+q\bar{q}q\bar{q}$	286.9	287.8
$e^-\gamma(\text{BS}) \rightarrow \nu q\bar{q}q\bar{q}$	136.9	262.5
$e^+\gamma(\text{BS}) \rightarrow \bar{\nu} q\bar{q}q\bar{q}$	136.4	262.3
$e^-\gamma(\text{EPA}) \rightarrow \nu q\bar{q}q\bar{q}$	32.6	54.2
$e^+\gamma(\text{EPA}) \rightarrow \bar{\nu} q\bar{q}q\bar{q}$	32.6	54.2
$e^-\gamma(\text{BS}) \rightarrow q\bar{q}H\nu\bar{\nu}$	15.8	58.6
$e^+\gamma(\text{BS}) \rightarrow q\bar{q}H\nu\bar{\nu}$	15.7	58.5
$e^-\gamma(\text{EPA}) \rightarrow q\bar{q}H\nu\bar{\nu}$	3.39	11.7
$e^+\gamma(\text{EPA}) \rightarrow q\bar{q}H\nu\bar{\nu}$	3.39	11.7
$\gamma(\text{BS})\gamma(\text{BS}) \rightarrow qq\bar{q}\bar{q}$	21406.2	13050.3
$\gamma(\text{BS})\gamma(\text{EPA}) \rightarrow qq\bar{q}\bar{q}$	4018.7	2420.6
$\gamma(\text{EPA})\gamma(\text{BS}) \rightarrow qq\bar{q}\bar{q}$	4034.8	2423.1
$\gamma(\text{EPA})\gamma(\text{EPA}) \rightarrow qq\bar{q}\bar{q}$	753.0	402.7

Table 7.1: List of signal and background samples with the corresponding cross sections at $\sqrt{s} = 3 \text{ TeV}$ and $\sqrt{s} = 1.4 \text{ TeV}$. q can u, d, s, b or t. Unless specified, q , ℓ and ν represent particles and its corresponding anti-particles. γ (BS) represents a real photon from beamstrahlung (BS). γ (EPA) represents a “quasi-real” photon, simulated with the Equivalent Photon Approximation. For processes involving Higgs production explicitly, simulated Higgs mass is 126 GeV. Otherwise, Higgs mass is set to 14 TeV. Simulated W has invariant mass of 80.385 GeV.

selection and background rejection. The latest function flavour tagging processor exist in iLCSoft v01-16, which prevented the usage of more recent iLCSoft.

For my signal channel, $HH \rightarrow b\bar{b}W^+W^-$, there is no lepton in the final state. Hence a effective lepton identifier would improve the signal identification. Processors are wither developed or optimised with samples at $\sqrt{s} = 1.4 \text{ TeV}$, and checked against samples at $\sqrt{s} = 3 \text{ TeV}$. Because the expected signal significance would be low, the processors are optimised to reject more background at the cost of losing a bit more signals, to increase the signal significance. It was found that the same set of parameters work well under $\sqrt{s} = 1.4 \text{ TeV}$ and 3 TeV .

7.5.1 Electron and muon identification

IsolatedLeptonFinderProcessor

In Marlin package, IsolatedLeptonFinderProcessor has been used. The optimal parameters ware chosen in collaboration and tested. The particle is identified as an isolated light lepton if it passes a chain of cuts.

A charge track is considered if it has more than 15 GeV energy. An electron is identified if the energy in the ECal is over 90% of the total calorimetric energy. A muon is identified if the energy in the ECal is between 5% and 25% of the total calorimetric energy. Furthermore, only primary track is selected, which requires the Euclidean distance in the x-y plane, the in z direction, and in the x-y-z three dimensional space of the track starting point to the impact point to be less than 0.02 mm , 0.03 mm , and 0.04 mm , respectively. The isolation criteria states that

$$E_{\text{cone}}^2 \leq 5.7 \times E_l - 50 \quad (7.1)$$

where, E_{cone} is the total energy of PFOs within an opening angle of $\cos^{-1}(0.995)$ of the light lepton, and E_l is the energy of the light lepton.

BonoLeptonFinderProcessor

The IsolatedLeptonFinderProcessor is rather conservative. I developed a new more aggressive light lepton selection processor, BonoLeptonFinderProcessor, that utilises calorimetric information provided by PandoraPFA.

The processor uses two chains of cuts.

First chain uses the particle ID information from PandoraPFA. A electron is identified if it is a “PandoraPFA” electron and the energy in the ECal is over 95% of the total calorimetric energy. A muon is identified if it is a “PandoraPFA” muon. Primary track selection states the Euclidean distance in the x-y-z three dimensional space of the track starting point to the impact point to be less than 0.015 mm, and the PFO energy is more than 10 GeV. The light lepton either satisfy the high p_T requirement of at least 40 GeV, or the isolation criteria,

$$E_l \geq 23 \times \sqrt{E_{\text{cone}}} + 5 \quad (7.2)$$

where E_{cone} and E_l have the same definition as in the IsolatedLeptonFinderProcessor.

Second chain of cuts is similar to the IsolatedLeptonFinderProcessor. An electron is identified if the energy in the ECal is over 95% of the total calorimetric energy. A muon is identified if the energy in the ECal is between 5% and 20% of the total calorimetric energy. Primary track selection states the Euclidean distance in the x-y-z three dimensional space of the track starting point to the impact point to be less than 0.5 mm, and the PFO energy is more than 10 GeV. The light lepton either satisfy the high p_T requirement of at least 40 GeV, or the isolation criteria,

$$E_l \geq 28 \times \sqrt{E_{\text{cone}}} + 30 \quad (7.3)$$

where, E_{cone} is the total energy of PFOs within an opening angle of $\cos^{-1}(0.99)$ of the light lepton, and E_l is the energy of the light lepton.

Comparison: IsolatedLeptonFinderProcessor v.s. BonoLeptonFinderProcessor

Two processors share similar criterion for light lepton identification. The main difference is that the BonoLeptonFinderProcessor allows high p_T light lepton to be identified in a potential non-isolated environment, which leads to the more aggressiveness of the BonoLeptonFinderProcessor. The performance of two processors on the signal and selected background samples is shown in table [7.2](#)

7.5.2 Tau identification

TauFinderProcessor

With a decay length of $87\mu\text{m}$, tau leptons decay before reaching the detector and can only be identified through the reconstruction of their decay products. The leptonic decay of tau can be identified using the two isolated lepton finder processor. Therefore tau identification will focus on the hadronic decay.

TauFinderProcessor [17], an existing processor Marlin package, has been tuned in collaboration and tested. The a collection of tau decay productions are identified they pass a chain of cuts.

Particles are not considered if p_T is less than 1 GeV or $|\cos(\theta_Z)|$ is more than 1.1 rad, as they are more likely from beam induced background. A seed is considered if a charged particle has p_T more than 10 GeV. A search cone of opening angle 0.03 rad is then formed. The search cone is rejected if it has more than 3 charged particles, more than 10 particles or its invariant mass more than 2 GeV. An isolation cone is formed with opening angle between 0.03 and 0.33 rad of the seed. The seed is rejected if there are more than 3 GeV in the isolation cone.

BonoTauFinderProcessor

The TauFinderProcessor's performance is decent, but there is room for improvement. I developed a new more aggressive tau lepton selection processor, BonoTauFinderProcessor, that utilises calorimetric information provided by PandoraPFA.

Similar to the previous processor, PFOs with p_T less than 1 GeV are rejected. A tau seed is defined as a charged particle with p_T at least 5 GeV. The search cone has an opening angle of $\cos^{-1}(0.999)$. Particles are iteratively added to the search cone according to the size of the opening angle to the seed. A temporary search cone is then considered if it has one or three charged particles, and the invariant mass is less than 3 GeV. The search cone needs to satisfy one of isolation criterion.

1. No particle in the large isolation cone, and p_T of search cone at least 10 GeV,
2. One charged particle in the search cone, one particle in the large isolation cone, and r_0 larger than 0.01 mm,

Selection / Efficiency (1.4 TeV)	Signal	$qqqq\ell\nu$
IsolatedLeptonFinderProcessor	99.3%	50.3%
BonoLeptonFinderProcessor	99.1%	39.9%
TauFinderProcessor	97.5%	52.3%
BonoTauFinderProcessor	89.7%	38.5%
ForwardFinderProcessor	98.9%	95.1%
Combined	86.6%	16.8%
Processor / Efficiency (3 TeV)	Signal	$qqqq\ell\nu$
IsolatedLeptonFinderProcessor	99.5%	66.8%
BonoLeptonFinderProcessor	99.0%	52.5%
TauFinderProcessor	97.7%	79.5%
BonoTauFinderProcessor	86.3%	60.3%
ForwardFinderProcessor	95.9%	80.7%
Combined	81.0%	23.3%

Table 7.2: isolated lepton finder processors performance on the signal and selected background samples.

3. Three charged particle in the search cone, one particle in the large isolation cone, p_T of search cone at least 10 GeV, and search cone opening angle less than $\cos^{-1}(0.9995)$,
4. One charged particle in the search cone, no particle in the small isolation cone, r_0 larger than 0.01 mm, and p_T of search cone at least 10 GeV,
5. Three charged particle in the search cone, no particle in the small isolation cone, p_T of search cone at least 10 GeV, and search cone opening angle less than $\cos^{-1}(0.9995)$,

where large and small isolation cone are defined as opening angle of $\cos^{-1}(0.95)$, and $\cos^{-1}(0.99)$ respectively. If there are multiple temporary search cone of a same seed passing the isolation criteria, the cone with smallest opening angle is chosen for output.

Comparison: TauFinderProcessor v.s. BonoTauFinderProcessor

Two processors share similar size of search cone and isolation cone. The BonoTauFinderProcessor has looser cut on minimum p_T and invariant, but stricter isolation criterion. This leads to a more aggressive tau finder. The performance of two processors on the signal and selected background samples is shown in table 7.2

7.5.3 Very forward electron identification

Certain background channels, for example photon-electron interactions, contain electrons in the very forward part of the detector, namely LCal and BCal. These forward calorimeters were not simulated due to computational limitation. Most particle in these detector would be very forward particles from beam induced background. However, previous study has shown [] that high energy electrons can be identified with high efficiency. Due to the lack of tracking in these region, electrons and photons would have the same electromagnetic shower profile, with the given calorimeter resolution. MC photons and electrons are checked if they fall in the LCal or the BCal, and checked against the known detection efficiency.

Beam Calorimeter acceptance is defined as $|\cos(\theta_Z)|$ is between 0.01 and 0.04 rad and length in z direction is between 3181 and 3441 mm. Luminosity Calorimeter acceptance is defined as $|\cos(\theta_Z)|$ is between 0.038 and 0.11 rad and length in z direction is between 2539 and 2714 mm. For $\sqrt{s} = (\text{TeV } 3)$, the BeamCal detection efficiency is provided by a software package []. For $\sqrt{s} = (\text{TeV } 1.4)$, the same software for the BeamCal is used, by scaling the energy of the MC particle by a factor of $\frac{3}{1.4}$. For the LumiCal, the identification efficiency is defined as

$$\varepsilon = \begin{cases} 0, & \text{if } E < 50 \text{ GeV} \\ 0.99 \times \frac{(\text{erf}(E-100)+1)}{2}, & \text{otherwise} \end{cases} \quad (7.4)$$

where E is the energy of the electron or the photon.

The background rejection is significant, shown in table ?? for the signal and selected background.

7.5.4 Other lepton identification processors

Other isolated lepton selection processors available in Marlin package, including IsolatedLeptonTagging and TauJetClustering, have been tested. The results, after some tuning of parameters, were unsatisfactory. They either performed poorly comparing to the processors above, or became redundant after the processors above. Therefore, these processors were not used in this analysis.

Selection / Efficiency (1.4 TeV)	Signal	$e^- \gamma(\text{BS}) \rightarrow e^- qqqq$
Combined light lepton finder	87.6%	67.5%
ForwardFinderProcessor	98.9%	53.6%
Combined	86.6%	30.8%
Processor / Efficiency (3 TeV)	Signal	$e^- \gamma(\text{BS}) \rightarrow e^- qqqq$
Combined light lepton finder	84.4%	72.7%
ForwardFinderProcessor	95.9%	55.4%
Combined	81.0%	33.4%

Table 7.3: Very forward electron and photon finder performance on the signal and selected background samples.

7.6 Jet reconstruction

The signal channel, $HH \rightarrow b\bar{b}W^+W^- \rightarrow b\bar{b}qqqq$, is a four-jet final state. A useful technique for the analysis is to reconstruct the four-jet final state using jet algorithms. This allows discriminative variables to be calculated.

7.6.1 Jet reconstruction optimisation

Longitudinal invariant, k_t , jet algorithm was chosen for the jet clustering. Due to the presence high level of beam induced background at the CLIC, it has been shown that a jet algorithm designed for hadron colliders are more effective than those traditional designed for the electron-positron collider, such as Durham algorithm. []

The free parameters for k_t algorithm is the R parameter, which controls the fatness of the jet. There is also the choice of the PFO collection, which incorporate different level of time and p_T cuts, to reduce beam induce background. Both parameters are optimised for $\sqrt{s} = 1.4$ TeV and $\sqrt{s} = 3$ TeV.

The details of jet algorithm can be found in section ??.

The R parameter of the k_t jet algorithm, and the collection of the PFOs are chosen to give the best invariant mass resolution. When there are a few suitable candidate, analysis were performed in parallel. Decision were made to give the highest signal significance.

k_t jet algorithm was used as part of the FastJet algorithms available in the Marlin package.

The samples containing the signal, $HH \rightarrow b\bar{b}W^+W^- \rightarrow b\bar{b}qqqq$, was used for the optimisation of the jet reconstruction. The signal events were chosen using MC truth information.

Jet algorithm was run in exclusive mode, where number of jets is chosen to be six.

For the signal, $HH \rightarrow b\bar{b}W^+W^- \rightarrow b\bar{b}qqqq$, one Higgs decays to two b quarks, resulting in two jets from hadronisation. Similarly the other Higgs decays to two W bosons, where each W boson decays into two quarks. Therefore, the expected number of jets is six.

Jets produced by the k_t jet algorithm are paired up using MC truth information, to the corresponding Higgs and W boson. Four invariant mass distributions are obtained: two Higgs masses, $m_{H_{bb}}$, $m_{H_{WW^*}}$, and two W masses m_W , m_{W^*} . W^* indicates the off-mass-shell W boson, because when a Higgs decays into two W bosons, one W is off the mass shell, as the Higgs mass is less than the sum two W masses.

Three mass distributions are worth comparing for different jet reconstruction, namely, $m_{H_{bb}}$, $m_{H_{WW^*}}$, and m_W . The ideal jet reconstruction should produce the a sharp mass peak around the particle's true mass.

To quantitatively access the mass distribution, a gaussian like fit is performed to extract the position of the peak, and the width of the distribution. The fit has the form:

$$f(m) = Ae^{-\frac{(m-\mu)^2}{g}} \begin{cases} g = 2\sigma_L + \alpha_L(m - \mu), & \text{if } m < \mu \\ g = 2\sigma_R + \alpha_R(m - \mu), & \text{if } m \geq \mu \end{cases} \quad (7.5)$$

The fit represents an asymmetrical gaussian function, where m is binned mass distribution, with 50 bins in range $[0, 200]$ GeV. The fitted mass peak is denoted by μ . σ_L and σ_R allow asymmetrical width of the distribution. α parameter controls the fit of tails. Inspired by the $t\bar{t}$ analysis [], the use of the α parameter allows the fit in the whole mass range, otherwise only the peak of the distribution should be fitted with a gaussian like function. A is the normalisation factor. An example of the fit of $m_{H_{bb}}$ is shown in figure 7.1.

For $\sqrt{s} = 1.4$ TeV, shown in figure 7.2, normal selected PFO with $R = 0.7$ give a good fitted mass for H_{WW^*} and W . The mass is slightly too low for the H_{bb} . figure 7.3 shows the combined relative fitted width for the H_{bb} , H_{WW^*} and W . Normal selected PFO with $R = 0.7$ gives an almost optimal relative width for H_{bb} , while achieving a good balance

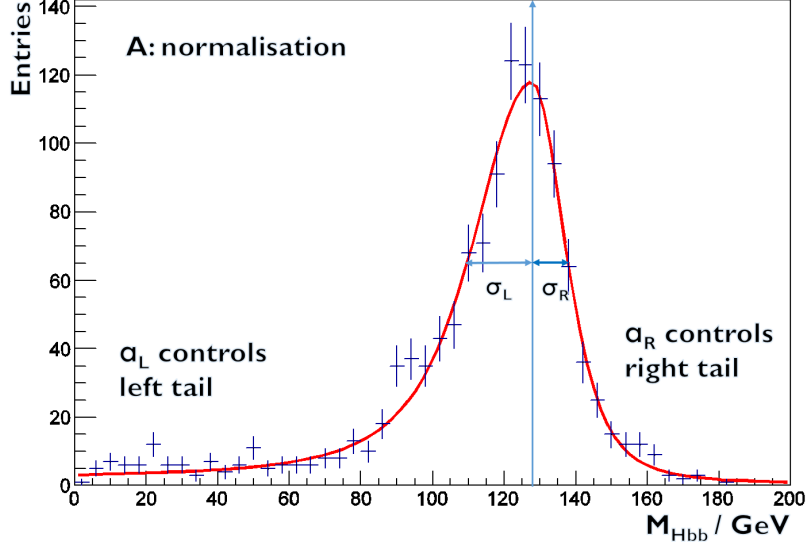


Figure 7.1: A typical example of MC mass fit of $m_{H_{bb}}$ for double higgs analysis. Red line indicates the best fit. Vertical arrow indicates the fitted peak position.

for H_{WW^*} and W . Therefore, normal selected PFO with $R = 0.7$ is chosen to be the optimal jet reconstruction parameters.

For $\sqrt{s} = 3 \text{ TeV}$, the choice is a bit more complicated. Shown in figure 7.4, fitted mass for H_{bb} favours normal selected PFO with $R = 0.8$. Fitted mass for H_{WW^*} favours tight selected PFO with $R = 0.9$. Fitted mass for W favours tight selected PFO with $R = 0.8$. Looking at the combined relative fitted width for the H_{bb} , H_{WW^*} and W , shown in figure 7.5, normal selected PFO gives a larger width than tight selected PFO. Within tight selected PFO, small R values provide a shaper width for H_{WW^*} and H_{bb} , but a broader width for W . Therefore, tight selected PFO with $R = 0.7$ and $R = 1$ are both chosen for parallel analysis.

Later it was shown that tight selected PFO with $R = 0.7$ gives a better signal significance. Therefore the optimal choice of jet reconstruction for $\sqrt{s} = 3 \text{ TeV}$ is tight selected PFO with $R = 0.7$.

The extracted fitted parameters of optimal jet reconstructions are summarised in table 7.4.

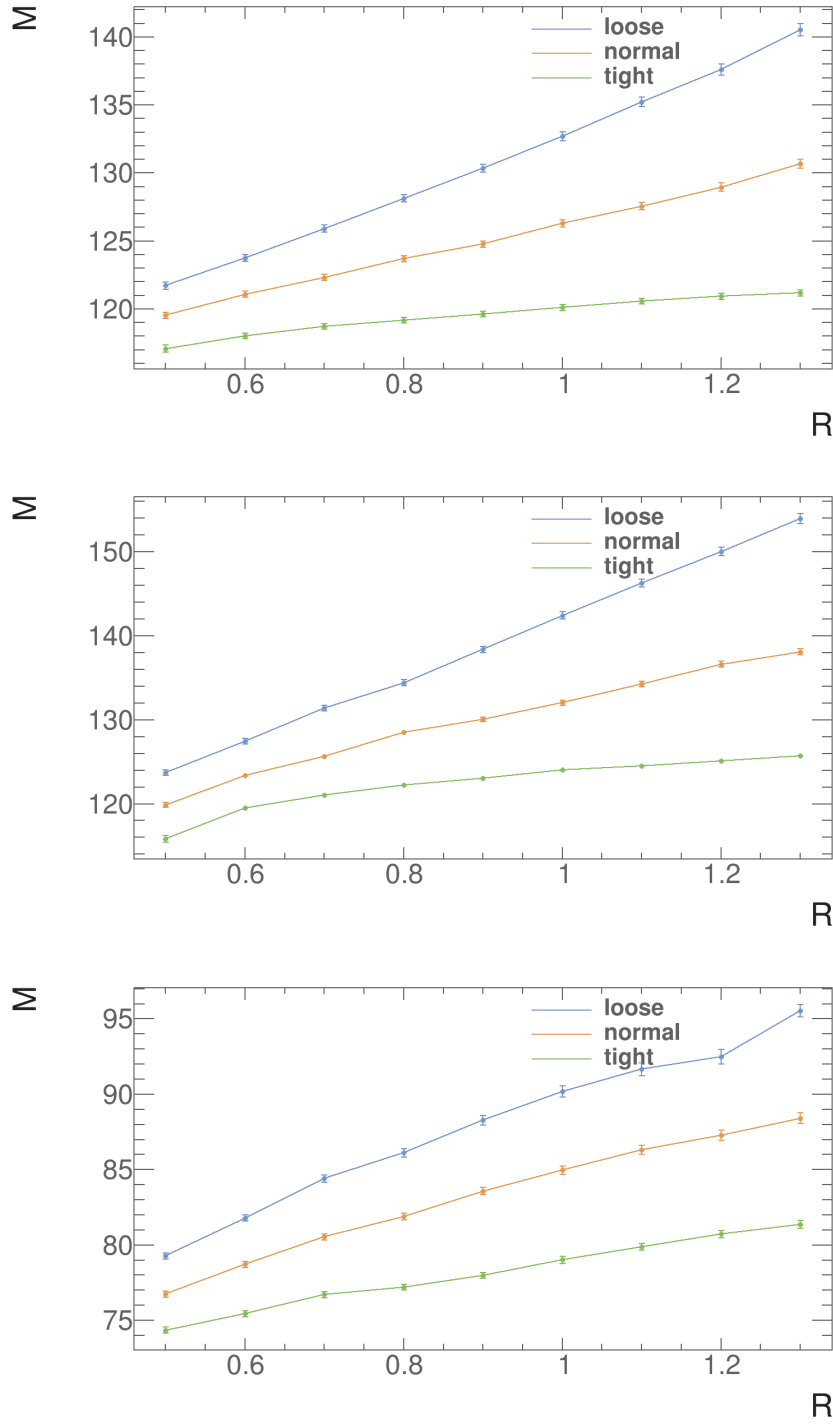


Figure 7.2: Fitted mass and statistical error of H_{bb} , H_{WW^*} and W for $\sqrt{s} = 1.4$ TeV, for loose, normal and tight selected PFO against R parameter.

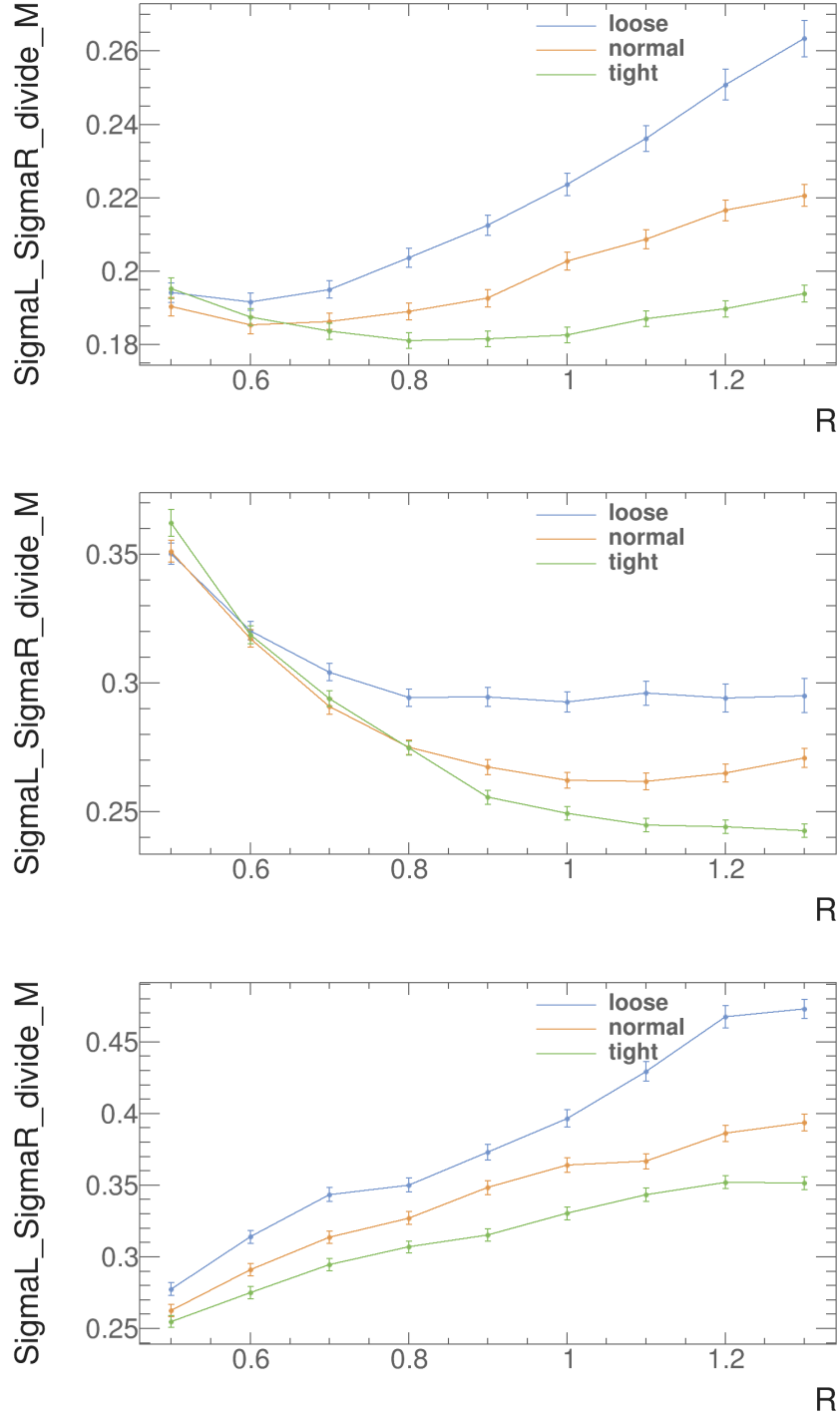


Figure 7.3: Fitted combined width and statistical error of H_{bb} , H_{WW^*} and W for $\sqrt{s} = 1.4$ TeV, for loose, normal and tight selected PFO against R parameter.

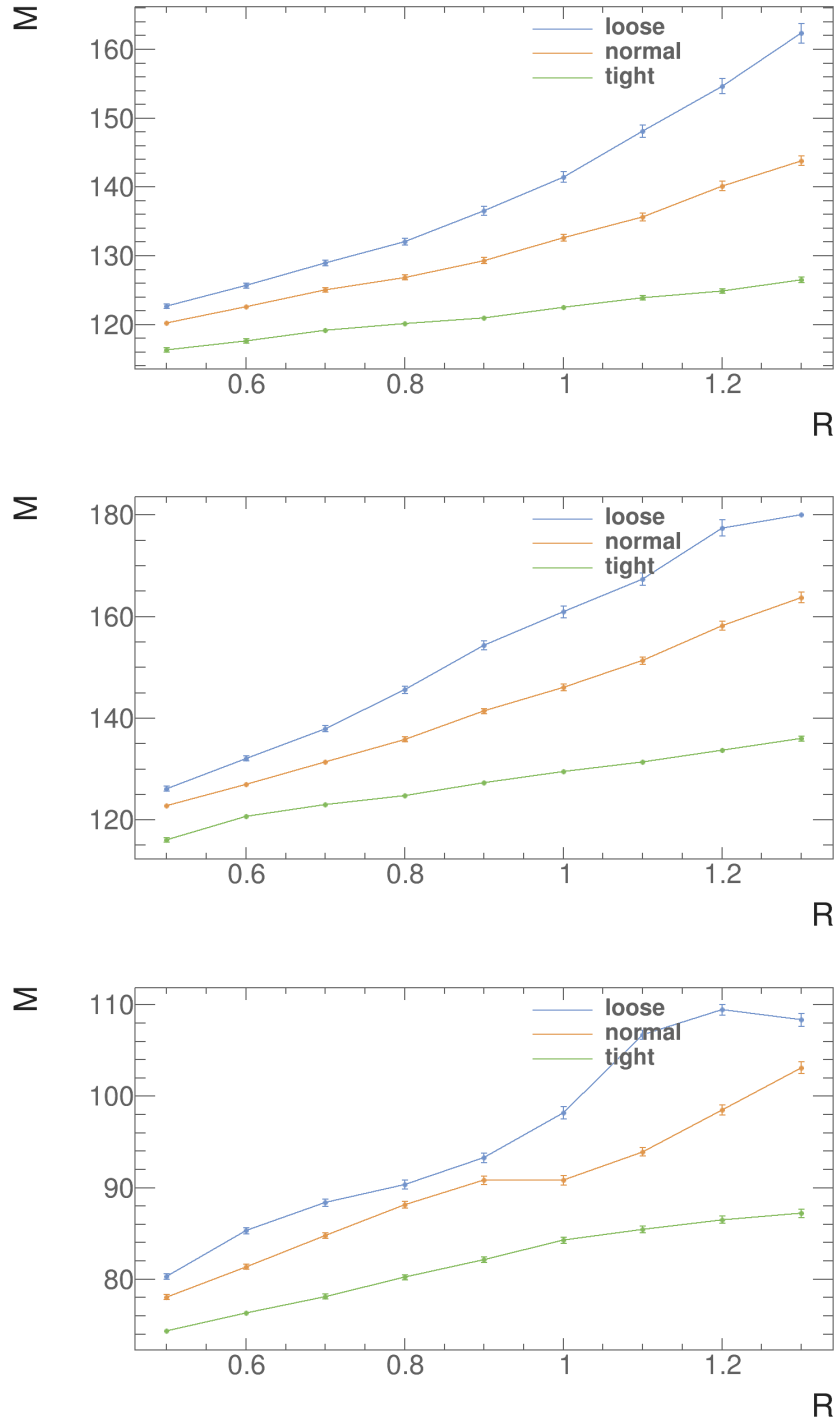


Figure 7.4: Fitted mass and statistical error of H_{bb} , H_{WW^*} and W for $\sqrt{s} = 3$ TeV, for loose, normal and tight selected PFO against R parameter.

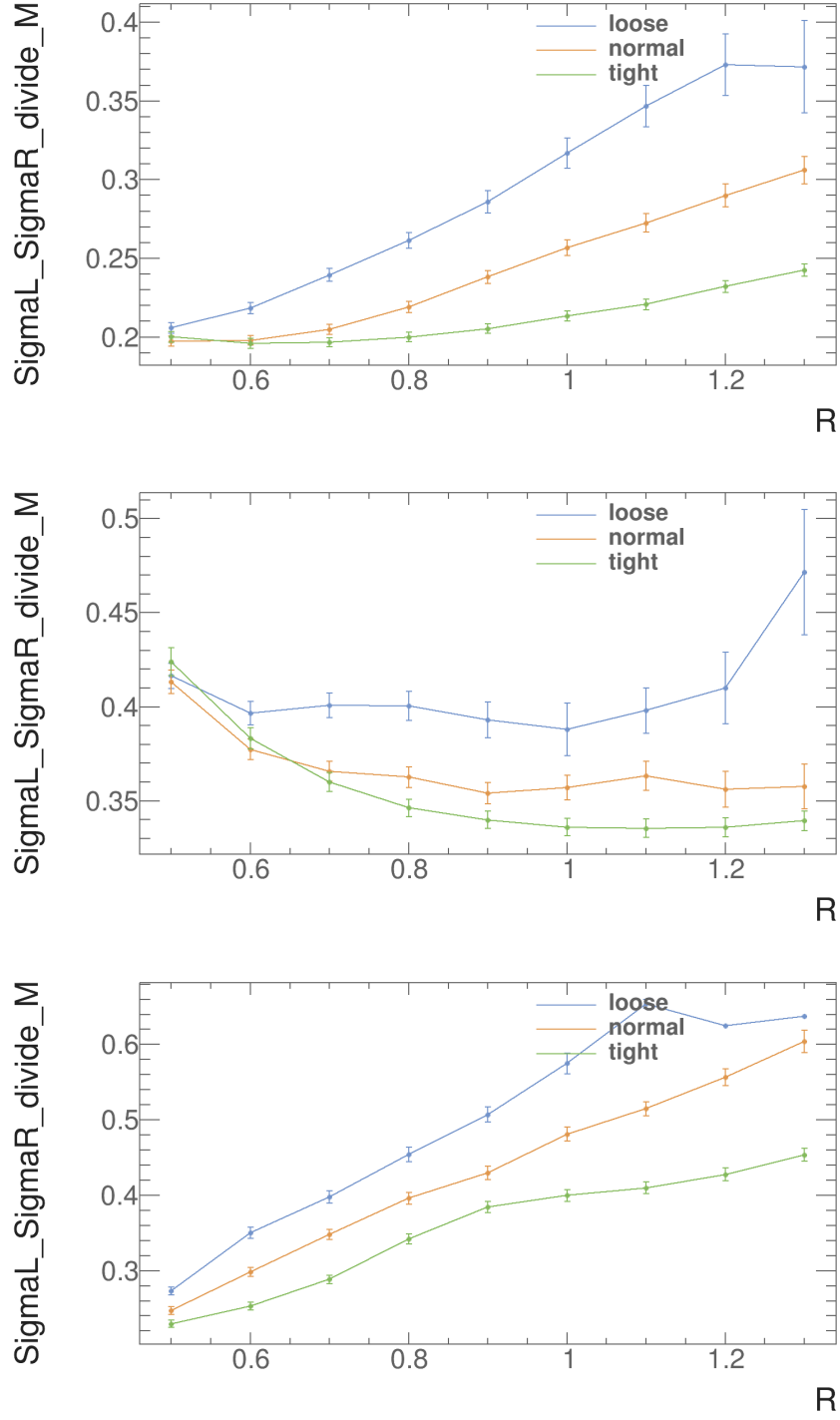


Figure 7.5: Fitted combined width and statistical error of H_{bb} , H_{WW^*} and W for $\sqrt{s} = 3$ TeV, for loose, normal and tight selected PFO against R parameter.

Jet Parameters	$\sqrt{s} = 1.4 \text{ TeV}$	$\sqrt{s} = S \text{ TeV}$
$\mu_{H_{bb}}$	$122.3_{\pm 0.2}$	$119.1_{\pm 0.3}$
$\sigma_{L,H_{bb}}$	$15.2_{\pm 0.2}$	$15.0_{\pm 0.3}$
$\sigma_{R,H_{bb}}$	$7.55_{\pm 0.16}$	$8.4_{\pm 0.2}$
$\mu_{H_{WW^*}}$	$125.7_{\pm 0.2}$	$123.0_{\pm 0.3}$
$\sigma_{L,H_{WW^*}}$	$29.4_{\pm 0.3}$	$36.6_{\pm 0.6}$
$\sigma_{R,H_{WW^*}}$	$7.18_{\pm 0.17}$	$7.4_{\pm 0.2}$
μ_W	$80.5_{\pm 0.2}$	$78.1_{\pm 0.3}$
$\sigma_{L,W}$	$16.2_{\pm 0.3}$	$13.1_{\pm 0.4}$
$\sigma_{R,W}$	$9.03_{\pm 0.16}$	$9.5_{\pm 0.2}$

Table 7.4: The extracted fitted parameters of optimal jet reconstructions, normal selected PFO with $R = 0.7$ for $\sqrt{s} = 1.4 \text{ TeV}$ and tight selected PFO with $R = 0.7$ for $\sqrt{s} = 3 \text{ TeV}$.

7.6.2 Jet flavour tagging

Two b-jets out of six jets in final states are identified with flavour tagging processors. The processor calculates a set of discriminatively variables for a jet. After training the MVA, the MVA is applied to jets to produce a likelihood for b-jet and c-jet. For details see section ??.

The existing LCFIPlus processor in Marlin package is used. The training sample of the flavour tagging processor is $e^-e^+ \rightarrow Z\nu\bar{\nu}$, where Z decays to $q_l\bar{q}_l$, $b\bar{b}$, or $c\bar{c}$ at $\sqrt{s} = 1.4 \text{ TeV}$ and $\sqrt{s} = 3 \text{ TeV}$, because they have similar event topology as the signal, and they have only two jets in the final state.

The selection efficiency of b-jets and c-jets with training samples are shown in figure ??. Flavour tagging performs better at low energy. Because at high energy, particles are more collimated and more difficult to separate.

7.6.3 Jet pairing

The jet pairing was performed by seeking combination of jets that are compatible with signal $HH \rightarrow b\bar{b}W^+W^-$.

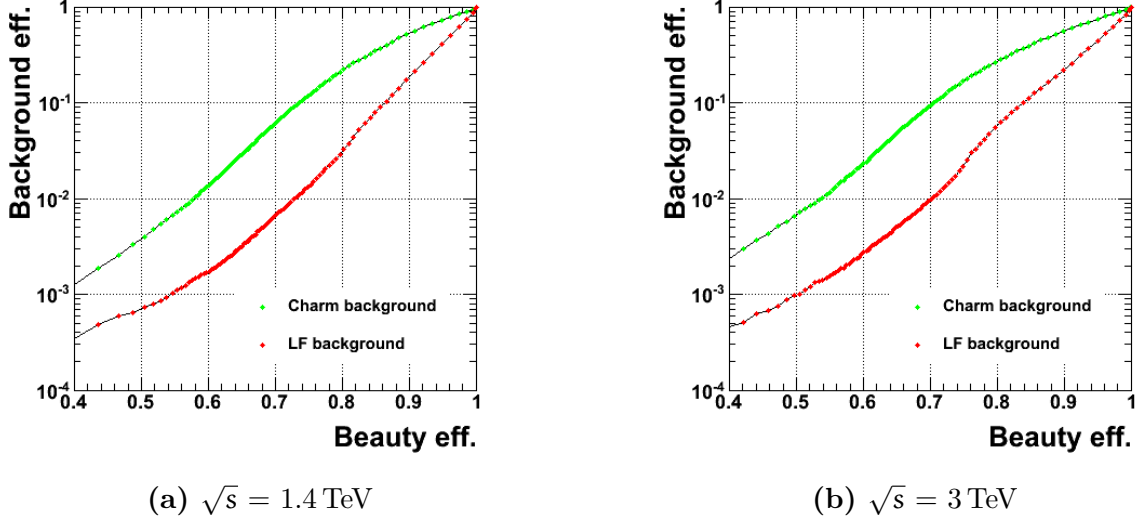


Figure 7.6: Performance of b-jet tagging with training samples

The actual pairing is done via a minimisation

$$\chi^2 = \left(\frac{m_{ij} - \mu_{H_{bb}}}{\sigma'_{H_{bb}}} \right)^2 + \left(\frac{m_{klmn} - \mu_{H_{WW^*}}}{\sigma'_{H_{WW^*}}} \right)^2 + \left(\frac{m_{kl} - \mu_W}{\sigma'_W} \right)^2, \quad (7.6)$$

where, $\mu_{H_{bb}}$ and $\sigma'_{H_{bb}}$ are the fitted invariant mass, and the fitted width, respectively. Both are obtained in section 7.6.1. $\sigma'_{H_{bb}}$ is $\sigma_{L,H_{bb}}$ when $m_{ij} < m_{H_{bb}}$, and $\sigma_{R,H_{bb}}$ otherwise. Similarly $\mu_{H_{WW^*}}$ and μ_W are fitted mass, and $\sigma'_{H_{WW^*}}$ and σ'_W are fitted invariant mass, and the fitted width, respectively. Out of the six jets from the jet clustering, indicated by subscript i, j, k, l, m, n , two are used for H_{bb} , two for W and four for H_{WW^*} . The fitted parameters used are listed in table 7.4. Additional requirement is that at least one of two jets forming H_{bb} needs to have a b-jet tag of 0.2 or greater.

With the χ^2 , all possible combinations are tested, and the one with smallest χ^2 is chosen.

7.7 Pre-selection

Discriminative variables were calculated. Some are used as to discard background events, whilst hurting the signal events a bit. This allows MVA to concentrate on events where it is difficult to separate in a single parameter space.

7.7.1 Discriminative pre-selection cuts

As discussed before, events with identified leptons are rejected. Jet pairing implies that events with the largest b-jet tag less than 0.2 are rejected.

For $\sqrt{s} = 1.4 \text{ TeV}$, a range of variables were tested and three were chosen as pre-selection cuts.

Event with invariant mass of two higgs less than 150 GeV is rejected. The cut above 120 GeV is needed as some background samples were generated only for invariant mass greater than 120 GeV. Shown in table ?? and figure ??, this cut is effective against samples with two quark final states.

Event with second highest b-jet tag less than 0.2 is rejected. This stricter cut than the jet pairing helps to reduce samples with no b-jets.

Event with p_T of two higgs less than 30 GeV is rejected. This is extremely effective against samples with no neutrinos in the final state.

For $\sqrt{s} = 3 \text{ TeV}$, event with invariant mass of two higgs less than 150 GeV is rejected, for the reason similar to $\sqrt{s} = 1.4 \text{ TeV}$.

In addition, event with highest b-jet tag less than 0.7 is rejected. It is found that b-jet tag is less efficient at a higher \sqrt{s} . Therefore, a stricter cut at b-jet tag is useful to compensate for the tagging efficiency loss.

These set of cuts are stricter than usual analysis. The cross sections of signal channel for both \sqrt{s} are extremely small, comparing to the background. Hence only the signal events with very clear characteristic topologies would be able to pass the final selection, in order to achieve a decent signal-to-background ratio. Therefore, a strict pre-selection cut would not hurt the final signal selection. On the contrary, final signal selection would benefit from MVA being able to focus the difficult background events, where their topologies are too similar to the signal events to separate in any single parameter space.

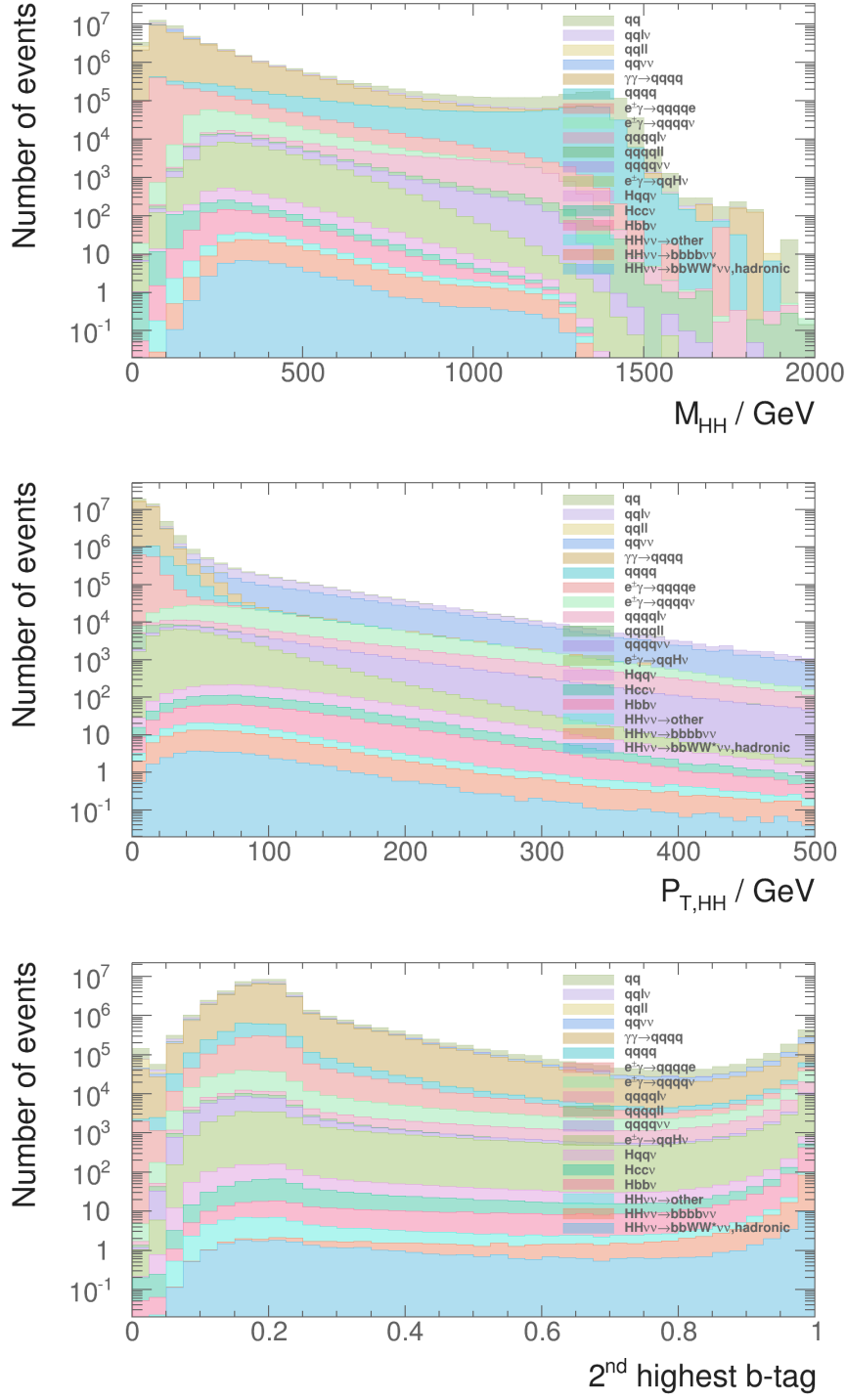


Figure 7.7: Discriminative pre-selection variables for $\sqrt{s} = 1.4$ TeV, after rejecting events with identified leptons, and jet pairing

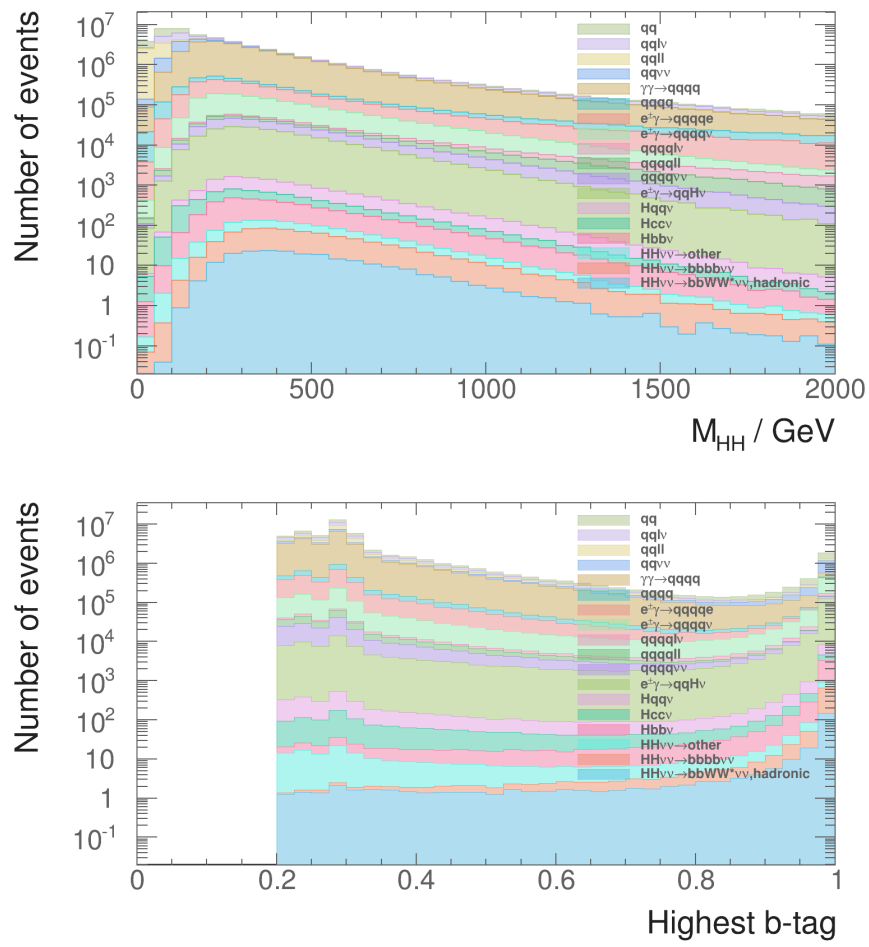


Figure 7.8: Discriminative pre-selection variables for $\sqrt{s} = 3 \text{ TeV}$, after rejecting events with identified leptons, and jet pairing

Channel / Efficiency $\sqrt{s} = 1.4 \text{ TeV}$	Expected number of events	Lepton ID and jet pair- ing	$m_{HH} > 150 \text{ GeV}$	$B_2 > 0.2$	$p_T > 30 \text{ GeV}$
$e^-e^+ \rightarrow HH\nu\bar{\nu} \rightarrow$ $b\bar{b}W^+W^-\nu\bar{\nu}$, hadronic	27.9	85.8%	85.6%	73.7%	66.4%
$e^-e^+ \rightarrow HH\nu\bar{\nu} \rightarrow$ $b\bar{b}b\bar{b}\nu\bar{\nu}$	67.6	90.8%	90.5%	90.1%	80.6%
$e^-e^+ \rightarrow HH\nu\bar{\nu} \rightarrow$ other	128.0	36.2%	35.3%	27.7%	24.7%
$e^-e^+ \rightarrow q_l q_l H\nu\bar{\nu}$	1304.0	60.7%	59.8%	44.9%	42.0%
$e^-e^+ \rightarrow c\bar{c}H\nu\bar{\nu}$	546.1	67.4%	57.7%	46.5%	43.4%
$e^-e^+ \rightarrow b\bar{b}H\nu\bar{\nu}$	463.0	73.9%	72.6%	68.7%	64.2%
$e^-e^+ \rightarrow qq\bar{q}\bar{q}$	1867650.0	48.8%	46.1%	17.3%	4.7%
$e^-e^+ \rightarrow qq\bar{q}q\ell\bar{\ell}$	93150.0	5.0%	4.9%	1.5%	0.3%
$e^-e^+ \rightarrow qq\bar{q}q\ell\nu$	165600.0	15.1%	15.1%	12.4%	11.4%
$e^-e^+ \rightarrow qq\bar{q}q\nu\bar{\nu}$	34800.0	50.7%	50.0%	20.1%	18.8%
$e^-e^+ \rightarrow qq$	6014250.0	54.5%	17.5%	8.4%	2.2%
$e^-e^+ \rightarrow qq\ell\nu$	6464550.0	14.1%	5.3%	2.0%	1.6%
$e^-e^+ \rightarrow qq\ell\bar{\ell}$	4088700.0	13.0%	1.1%	0.6%	0.1%
$e^-e^+ \rightarrow qq\nu\nu$	1181550.0	60.1%	12.3%	6.2%	5.8%
$e^-\gamma(\text{BS}) \rightarrow e^-qq\bar{q}q$	1305787.5	23.3%	10.6%	4.4%	0.4%
$e^+\gamma(\text{BS}) \rightarrow e^+qq\bar{q}q$	1300837.5	23.4%	10.5%	4.3%	0.4%
$e^-\gamma(\text{EPA}) \rightarrow e^-qq\bar{q}q$	430650.0	11.1%	5.4%	2.2%	0.3%
$e^+\gamma(\text{EPA}) \rightarrow e^+qq\bar{q}q$	430350.0	11.1%	5.3%	2.1%	0.3%
$e^-\gamma(\text{BS}) \rightarrow \nu qq\bar{q}q$	89775.0	58.3%	56.8%	31.0%	27.7%
$e^+\gamma(\text{BS}) \rightarrow \bar{\nu} qq\bar{q}q$	89212.5	57.6%	56.1%	30.3%	27.3%
$e^-\gamma(\text{EPA}) \rightarrow \nu qq\bar{q}q$	26100.0	29.6%	28.9%	15.4%	13.9%
$e^+\gamma(\text{EPA}) \rightarrow \bar{\nu} qq\bar{q}q$	25950.0	29.2%	28.5%	15.0%	13.7%
$e^-\gamma(\text{BS}) \rightarrow qqH\nu\nu$	1241.0	61.2%	60.0%	45.4%	34.5%
$e^+\gamma(\text{BS}) \rightarrow qqH\nu\nu$	1232.8	61.2%	60.0%	45.4%	34.2%
$e^-\gamma(\text{EPA}) \rightarrow qqH\nu\nu$	354.7	31.9%	31.3%	23.8%	18.2%
$e^+\gamma(\text{EPA}) \rightarrow qqH\nu\nu$	355.1	32.2%	31.7%	23.9%	18.7%
$\gamma(\text{BS})\gamma(\text{BS}) \rightarrow qq\bar{q}q$	2054951.5	56.3%	23.9%	9.6%	0.3%
$\gamma(\text{BS})\gamma(\text{EPA}) \rightarrow qq\bar{q}q$	4521037.5	33.6%	14.2%	5.7%	0.4%
$\gamma(\text{EPA})\gamma(\text{BS}) \rightarrow qq\bar{q}q$	4539150.0	33.7%	14.2%	5.7%	0.4%
$\gamma(\text{EPA})\gamma(\text{EPA}) \rightarrow qq\bar{q}q$	1129500.0	21.1%	9.1%	3.7%	0.4%

Table 7.5: List of signal and background samples with the corresponding expected number at $\sqrt{s} = 1.4 \text{ TeV}$, assuming a luminosity of 1500 fb^{-1} . The selection efficiencies are presented in a “flow” fashion, as the every selection cut contains all the cuts to the left of it.

Channel / Efficiency $\sqrt{s} = 3 \text{ TeV}$	Expected number of events	Lepton ID and jet pair- ing	$m_{HH} > 150 \text{ GeV}$	$B_1 > 0.7$
$e^-e^+ \rightarrow HH\nu\bar{\nu} \rightarrow$ $b\bar{b}W^+W^-\nu\bar{\nu}$, hadronic	146.0	80.2%	79.9%	69.7%
$e^-e^+ \rightarrow HH\nu\bar{\nu} \rightarrow$ $b\bar{b}b\bar{b}\nu\bar{\nu}$	355.0	83.4%	82.9%	81.2%
$e^-e^+ \rightarrow HH\nu\bar{\nu} \rightarrow$ other	675.0	36.7%	35.8%	25.2%
$e^-e^+ \rightarrow q_l q_l H\nu\bar{\nu}$	6115.4	59.5%	58.5%	40.4%
$e^-e^+ \rightarrow c\bar{c}H\nu\bar{\nu}$	2249.9	64.8%	58.4%	39.3%
$e^-e^+ \rightarrow b\bar{b}H\nu\bar{\nu}$	2197.7	69.7%	68.4%	64.2%
$e^-e^+ \rightarrow qq\bar{q}q$	1093000.0	48.5%	39.7%	3.0%
$e^-e^+ \rightarrow qq\bar{q}q\ell\ell$	338600.0	14.7%	14.2%	0.7%
$e^-e^+ \rightarrow qq\bar{q}q\ell\nu$	213200.0	19.7%	19.4%	10.0%
$e^-e^+ \rightarrow qq\bar{q}q\nu\bar{\nu}$	143000.0	58.4%	57.3%	11.9%
$e^-e^+ \rightarrow q\bar{q}$	5897800.0	62.8%	13.2%	2.7%
$e^-e^+ \rightarrow q\bar{q}\ell\nu$	11121800	28.3%	11.9%	0.3%
$e^-e^+ \rightarrow q\bar{q}\ell\ell$	6639200.0	38.3%	2.9%	0.7%
$e^-e^+ \rightarrow q\bar{q}\nu\nu$	2635000.0	71.4%	24.1%	5.3%
$e^-\gamma(BS) \rightarrow e^-qq\bar{q}q$	2004388.1	23.3%	21.5%	0.8%
$e^+\gamma(BS) \rightarrow e^+qq\bar{q}q$	2002334.1	23.4%	21.6%	0.8%
$e^-\gamma(EPA) \rightarrow e^-qq\bar{q}q$	575600.0	12.0%	11.0%	0.5%
$e^+\gamma(EPA) \rightarrow e^+qq\bar{q}q$	575600.0	12.0%	10.9%	0.4%
$e^-\gamma(BS) \rightarrow \nu qq\bar{q}q$	414750.0	61.7%	59.5%	20.4%
$e^+\gamma(BS) \rightarrow \bar{\nu} qq\bar{q}q$	414434.0	61.2%	59.1%	19.4%
$e^-\gamma(EPA) \rightarrow \nu qq\bar{q}q$	108400.0	30.9%	29.9%	9.6%
$e^+\gamma(EPA) \rightarrow \bar{\nu} qq\bar{q}q$	108400.0	30.7%	29.7%	9.1%
$e^-\gamma(BS) \rightarrow q\bar{q}H\nu\nu$	92588.0	58.3%	56.2%	37.3%
$e^+\gamma(BS) \rightarrow q\bar{q}H\nu\nu$	92430.0	58.1%	56.0%	37.1%
$e^-\gamma(EPA) \rightarrow q\bar{q}H\nu\nu$	23400.0	30.1%	29.2%	19.4%
$e^+\gamma(EPA) \rightarrow q\bar{q}H\nu\nu$	23400.0	29.7%	28.6%	18.8%
$\gamma(BS)\gamma(BS) \rightarrow qq\bar{q}q$	18009413.9	54.2%	49.2%	1.9%
$\gamma(BS)\gamma(EPA) \rightarrow qq\bar{q}q$	3824548.1	33.5%	30.2%	1.2%
$\gamma(EPA)\gamma(BS) \rightarrow qq\bar{q}q$	3828498.1	33.7%	30.3%	1.2%
$\gamma(EPA)\gamma(EPA) \rightarrow qq\bar{q}q$	805400.0	22.0%	19.8%	0.8%

Table 7.6: List of signal and background samples with the corresponding expected number at $\sqrt{s} = 3 \text{ TeV}$, assuming a luminosity of 2000 fb^{-1} . The selection efficiencies are presented in a “flow” fashion, as the every selection cut contains all the cuts to the left of it.

7.7.2 Sanity cuts

A set of very loose cuts, aiming to reduce the range of some discriminative variables to increase the effectiveness of MVA. (See section ?? on MVA) These cuts are very loose and physics motivated.

For $\sqrt{s} = 1.4 \text{ TeV}$, invariant masses for H_{bb} , H_{WW^*} , W , and HH are smaller than 500, 800, 200, and 1400 GeV, respectively.

For $\sqrt{s} = 3 \text{ TeV}$, invariant masses for H_{bb} , H_{WW^*} , W , and HH are smaller than 500, 800, 200, and 3000 GeV, respectively.

The selection efficiencies after sanity cuts and other pre-selection cuts stated above, are listed in table ??.

7.7.3 Mutually exclusive cuts for $HH \rightarrow b\bar{b}W^+W^-$ and $HH \rightarrow b\bar{b}b\bar{b}$

Since the analysis for $e^-e^+ \rightarrow HH\nu\bar{\nu}$ channel is divided into two subchannels, $HH \rightarrow b\bar{b}W^+W^- \rightarrow b\bar{b}qqqq$ and $HH \rightarrow b\bar{b}b\bar{b}$, it is convenient to divided samples, both signal and background, into two mutually exclusive sets. This will make combining subchaneels much easier, as correlations between subchannels do not need to be considered.

The most distinctive difference between two subchannels, is that they have different number of jets, and different number of b-jets in the final state. So variables related to number of b-jets or a number of jets are suitable for separating two subchannels.

Shown in figure 7.9, two subchannels can be clearly separated in the two dimensional parameter space. The optimal rectangular cuts were selected by scanning the two parameters, and maximising

$$\varepsilon = P(\text{subchannel}_1|\text{selection}) \times P(\text{subchannel}_2|\neg\text{selection}) \quad (7.7)$$

where **selection** represents the mutually exclusive cuts, $\neg\text{selection}$ indicates the phase space not covered by the **selection**.

Variables tested includes $\Sigma B_{4\text{jets}}$, $\sum_1^3 B_{4\text{jets}}$, y_{34} , y_{45} , y_{56} , y_{67} and other related variables. The best separation was summarised in table 7.7.

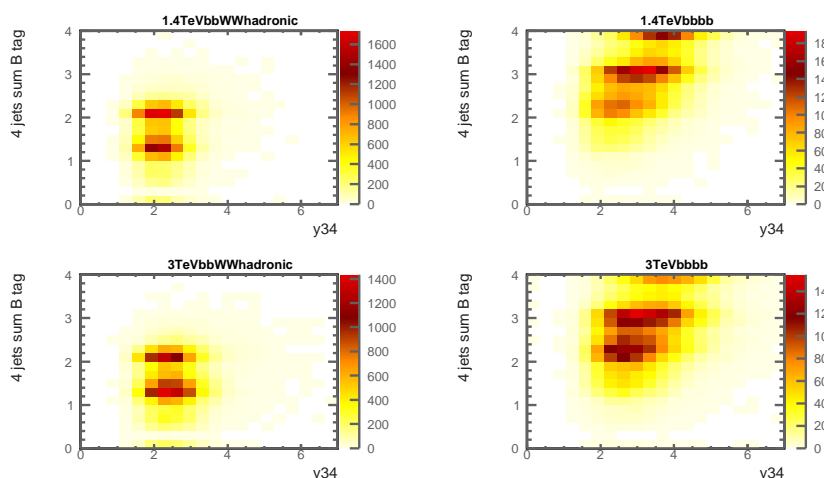


Figure 7.9: Sum of b tag against y_{34} , shown for signal samples

\sqrt{s}	selection	$HH \rightarrow b\bar{b}q\bar{q}q\bar{q}$ Selection Efficiency	$HH \rightarrow b\bar{b}b\bar{b}$ Selection Efficiency
1.4 TeV	$\Sigma B_{4\text{jets}} < 2.3$ and $y_{34} < 3.7$	86%	78%
3 TeV	$\Sigma B_{4\text{jets}} < 2.3$ and $y_{34} < 3.6$	89%	82%

Table 7.7: Mutually exclusive cuts, for full signal samples

The selection efficiencies after mutually exclusive cuts and other pre-selection cuts stated above, are listed in table ??.

7.8 Discriminative Variables

A series of discriminative variables were calculated, and fed into MVA for signal selection.

The full list of variables can be found in table ?. Same set of variables are used for $\sqrt{s} = 1.4 \text{ TeV}$ and $\sqrt{s} = 3 \text{ TeV}$.

figure ?? shows the the variable XX which gives a good discrimination of signal against background.

The optimal set were chosen to give the best MVA performance, whilst no strong pair-wise correlation between any two variables, shown in figure ??.

Channel / Efficiency	Sanity \sqrt{s} = 1.4 TeV	Mutually exclusive \sqrt{s} 1.4 TeV	Sanity \sqrt{s} = 3 TeV	Mutually exclusive \sqrt{s} = 3 TeV
$e^-e^+ \rightarrow HH\nu\bar{\nu} \rightarrow$ $b\bar{b}W^+W^-\nu\bar{\nu}$, hadronic	66.4%	59.7%	69.5%	61.7%
$e^-e^+ \rightarrow HH\nu\bar{\nu} \rightarrow$ $b\bar{b}b\bar{b}\nu\bar{\nu}$	80.6%	15.4%	81.1%	18.8%
$e^-e^+ \rightarrow HH\nu\bar{\nu} \rightarrow$ other	24.7%	20.5%	25.1%	20.0%
$e^-e^+ \rightarrow q_l q_l H\nu\bar{\nu}$	42.0%	39.5%	40.3%	35.9%
$e^-e^+ \rightarrow c\bar{c}H\nu\bar{\nu}$	43.4%	31.7%	39.2%	26.2%
$e^-e^+ \rightarrow b\bar{b}H\nu\bar{\nu}$	64.2%	25.2%	64.2%	25.9%
$e^-e^+ \rightarrow qq\bar{q}\bar{q}$	4.6%	3.4%	2.5%	1.4%
$e^-e^+ \rightarrow qq\bar{q}\bar{q}\ell\ell$	3.3%	3.1%	0.7%	0.6%
$e^-e^+ \rightarrow qq\bar{q}\bar{q}\ell\nu$	11.4%	9.8%	9.2%	7.2%
$e^-e^+ \rightarrow qq\bar{q}\bar{q}\nu\bar{\nu}$	18.8%	16.6%	11.8%	9.0%
$e^-e^+ \rightarrow qq$	2.0%	0.8%	2.5%	1.4%
$e^-e^+ \rightarrow qq\ell\nu$	1.6%	0.9%	0.3%	0.1%
$e^-e^+ \rightarrow qq\ell\ell$	0.1%	0.1%	0.7%	0.4%
$e^-e^+ \rightarrow qq\nu\nu$	5.8%	4.0%	5.3%	3.1%
$e^-\gamma(\text{BS}) \rightarrow e^-\bar{q}q\bar{q}q$	0.4%	0.3%	0.8%	0.7%
$e^+\gamma(\text{BS}) \rightarrow e^+\bar{q}q\bar{q}q$	0.4%	0.4%	0.8%	0.7%
$e^-\gamma(\text{EPA}) \rightarrow e^-\bar{q}q\bar{q}q$	0.3%	0.2%	0.4%	0.4%
$e^+\gamma(\text{EPA}) \rightarrow e^+\bar{q}q\bar{q}q$	0.3%	0.3%	0.4%	0.3%
$e^-\gamma(\text{BS}) \rightarrow \nu\bar{q}q\bar{q}q$	27.7%	25.3%	20.3%	16.8%
$e^+\gamma(\text{BS}) \rightarrow \bar{\nu}q\bar{q}\bar{q}q$	27.3%	24.9%	19.3%	15.9%
$e^-\gamma(\text{EPA}) \rightarrow \nu\bar{q}q\bar{q}q$	13.9%	12.6%	9.4%	7.8%
$e^+\gamma(\text{EPA}) \rightarrow \bar{\nu}q\bar{q}\bar{q}q$	13.7%	12.3%	8.9%	7.3%
$e^-\gamma(\text{BS}) \rightarrow qqH\nu\nu$	34.5%	30.2%	37.2%	30.2%
$e^+\gamma(\text{BS}) \rightarrow qqH\nu\nu$	34.2%	30.3%	37.1%	30.2%
$e^-\gamma(\text{EPA}) \rightarrow qqH\nu\nu$	18.2%	16.0%	19.0%	15.7%
$e^+\gamma(\text{EPA}) \rightarrow qqH\nu\nu$	18.7%	16.4%	18.4%	15.2%
$\gamma(\text{BS})\gamma(\text{BS}) \rightarrow qq\bar{q}\bar{q}$	0.3%	0.3%	1.9%	1.7%
$\gamma(\text{BS})\gamma(\text{EPA}) \rightarrow qq\bar{q}\bar{q}$	0.4%	0.3%	1.1%	1.0%
$\gamma(\text{EPA})\gamma(\text{BS}) \rightarrow qq\bar{q}\bar{q}$	0.4%	0.3%	1.1%	1.0%
$\gamma(\text{EPA})\gamma(\text{EPA}) \rightarrow qq\bar{q}\bar{q}$	0.4%	0.3%	0.7%	0.6%

Table 7.8: List of signal and background samples with the corresponding expected number at $\sqrt{s} = 1.4$ TeV and $\sqrt{s} = 3$ TeV, assuming a luminosity of 1500 and 2000 fb⁻¹, respectively. The selection efficiencies are presented in a “flow” fashion, as the every selection cut contains all the cuts to the left of it.

Variable	Description
$m_{H_{bb}}$	Invariant mass of H_{bb}
$m_{H_{WW^*}}$	Invariant mass of H_{WW^*}
m_W	Invariant mass of W
m_{HH}	Invariant mass of HH
E_{W^*}	Energy of W^*
E_{mis}	Missing energy, assuming collision at \sqrt{s}
$p_{TH_{bb}}$	Transverse momentum of H_{bb}
$p_{TH_{WW^*}}$	Transverse momentum of H_{WW^*}
p_{THH}	Transverse momentum of HH
η_{mis}	Pseudorapidity of missing momentum, assuming collision at \sqrt{s}
p_{THH}	Transverse momentum of HH
$-\ln(y_{23})$	minus \ln of y_{23} . See section ?? for y parameter. See section ?? for the \ln transformation
$-\ln(y_{34})$	minus \ln of y_{34} .
$-\ln(y_{45})$	minus \ln of y_{45} .
$-\ln(y_{56})$	minus \ln of y_{56} .
$B_{1,H_{bb}}$	Highest b-jet tag value of two jets forming H_{bb} .
$B_{2,H_{bb}}$	Lowest b-jet tag value of two jets forming H_{bb} .
$B_{1,W}$	Highest b-jet tag value of two jets forming W .
B_{1,W^*}	Highest b-jet tag value of two jets forming W^* .
$C_{1,H_{bb}}$	Highest c-jet tag value of two jets forming H_{bb} .
$C_{1,W}$	Highest c-jet tag value of two jets forming W .
$ \mathbf{S} $	Modulus of sphericity, \mathbf{S} . See section ??.
$\text{acol}_{H_{bb}}$	Acolinearity of two jets forming H_{bb} .
acol_W	Acolinearity of two jets forming W .
acol_{HH}	Acolinearity of H_{bb} and H_{WW^*} .
$N_{H_{bb}}$	Number of PFOs forming H_{bb} .
$N_{H_{WW^*}}$	Number of PFOs forming H_{WW^*} .
N_W	Number of PFOs forming W .
N_{W^*}	Number of PFOs forming W^* .
$\cos(\theta_{H_{bb}}^*)$	Cosine of opening angles of two jets forming H_{bb} , in their rest frame.
$\cos(\theta_{H_{WW^*}}^*)$	Cosine of opening angles of W and W^* , forming H_{WW^*} , in their rest frame.
$\cos(\theta_W^*)$	Cosine of opening angles of two jets forming W , in their rest frame.
$\cos(\theta_{W^*}^*)$	Cosine of opening angles of two jets forming W^* , in their rest frame.

7.9 Multivariate analysis

Multivariate analysis was performed with TMVA package. The classifier that performs the best was found to be the boosted decision tree. See section ?? for details on boosted decision tree.

The parameters for boosted decision tree were optimised and checked for overtraining. The most important variables are the depth of the tree and the number of trees. Other parameters includes the minimum number of nodes in a leaf, the number of cuts of a variable, the learning rate, the sampling fraction, the yes/no or purity leaf, adaBoost or gradient boost.

The optimisation and overtraining test was done with $\sqrt{s} = 3 \text{ TeV}$ samples. $\sqrt{s} = 1.4 \text{ TeV}$ samples produce similar results.

Half of the samples were used for training, and the other half used for testing.

7.10 Signal selection results

7.11 Couplings extration

Colophon

This thesis was made in $\text{\LaTeX} 2_{\epsilon}$ using the “hepthesis” class [\[18\]](#).

Bibliography

- [1] G. Sterman and S. Weinberg, Phys. Rev. Lett. **39**, 1436 (1977).
- [2] S. Moretti, L. Lonnblad, and T. Sjostrand, JHEP **08**, 001 (1998), hep-ph/9804296.
- [3] G. P. Salam, Eur. Phys. J. **C67**, 637 (2010), 0906.1833.
- [4] A. Ali and G. Kramer, Eur. Phys. J. **H36**, 245 (2011), 1012.2288.
- [5] M. Cacciari, G. P. Salam, and G. Soyez, Eur. Phys. J. **C72**, 1896 (2012), 1111.6097.
- [6] M. Cacciari and G. P. Salam, Phys. Lett. **B641**, 57 (2006), hep-ph/0512210.
- [7] S. Catani, Y. L. Dokshitzer, M. H. Seymour, and B. R. Webber, Nucl. Phys. **B406**, 187 (1993).
- [8] S. D. Ellis and D. E. Soper, Phys. Rev. **D48**, 3160 (1993), hep-ph/9305266.
- [9] S. Catani, Y. L. Dokshitzer, M. Olsson, G. Turnock, and B. R. Webber, Phys. Lett. **B269**, 432 (1991).
- [10] L. Linssen, A. Miyamoto, M. Stanitzki, and H. Weerts, (2012), 1202.5940.
- [11] M. Battaglia and F. P., CERN Report No. LCD-Note-2010-006, 2010 (unpublished).
- [12] M. Boronat, J. Fuster, I. Garcia, E. Ros, and M. Vos, Phys. Lett. **B750**, 95 (2015), 1404.4294.
- [13] T. Suehara and T. Tanabe, Nucl. Instrum. Meth. **A808**, 109 (2016), 1506.08371.
- [14] Linear Collider ILD Concept Group -, T. Abe *et al.*, (2010), 1006.3396.
- [15] H. Aihara *et al.*, (2009), 0911.0006.
- [16] A. Hocker *et al.*, PoS **ACAT**, 040 (2007), physics/0703039.
- [17] A. Míznich, CERN Report No. LCD-Note-2010-009, 2010 (unpublished).

- [18] A. Buckley, The hepthesis L^AT_EX class.

List of figures

7.1	Example MC mass fit for double higgs analysis	30
7.2	Fitted mass of H_{bb} , H_{WW^*} and W for $\sqrt{s} = 1.4 \text{ TeV}$	31
7.3	Fitted width of H_{bb} , H_{WW^*} and W for $\sqrt{s} = 1.4 \text{ TeV}$	32
7.4	Fitted mass of H_{bb} , H_{WW^*} and W for $\sqrt{s} = 3 \text{ TeV}$	33
7.5	Fitted width of H_{bb} , H_{WW^*} and W for $\sqrt{s} = 3 \text{ TeV}$	34
7.6	Performance of b-jet tagging with training samples	36
7.7	Discriminative pre-selection variables for $\sqrt{s} = 1.4 \text{ TeV}$	38
7.8	Discriminative pre-selection variables for $\sqrt{s} = 3 \text{ TeV}$	39
7.9	Sum of b tag against y_{34}	43

List of tables

7.1	List of signal and background samples with the corresponding cross sections at $\sqrt{s} = 3 \text{ TeV}$ and $\sqrt{s} = 1.4 \text{ TeV}$. q can u, d, s, b or t. Unless specified, q , ℓ and ν represent particles and its corresponding anti-particles. γ (BS) represents a real photon from beamstrahlung (BS). γ (EPA) represents a “quasi-real” photon, simulated with the Equivalent Photon Approximation. For processes involving Higgs production explicitly, simulated Higgs mass is 126 GeV. Otherwise, Higgs mass is set to 14 TeV. Simulated W has invariant mass of 80.385 GeV.	22
7.2	isolated lepton finder processors performance on the signal and selected background samples.	26
7.3	Very forward electron and photon finder performance on the signal and selected background samples.	28
7.4	The extracted fitted parameters of optimal jet reconstructions	35
7.5	List of signal and background samples with the corresponding expected number at $\sqrt{s} = 1.4 \text{ TeV}$, assuming a luminosity of 1500 fb^{-1} . The selection efficiencies are presented in a “flow” fashion, as the every selection cut contains all the cuts to the left of it.	40
7.6	List of signal and background samples with the corresponding expected number at $\sqrt{s} = 3 \text{ TeV}$, assuming a luminosity of 2000 fb^{-1} . The selection efficiencies are presented in a “flow” fashion, as the every selection cut contains all the cuts to the left of it.	41
7.7	Mutually exclusive cuts	43

7.8	List of signal and background samples with the corresponding expected number at $\sqrt{s} = 1.4$ TeV and $\sqrt{s} = 3$ TeV, assuming a luminosity of 1500 and 2000fb^{-1} , respectively. The selection efficiencies are presented in a “flow” fashion, as the every selection cut contains all the cuts to the left of it.	44
7.9	List of variables used in MVA	45